Journal of Molecular Spectroscopy **208,** 32–42 (2001)
doi:10.1006/jmsp.2001.8373, available online at http://www.idealibrary.com on IDEAL®

The Water Vapor Spectrum in the Region 8600–15 000 cm^{-1}: Experimental and Theoretical Studies for a New Spectral Line Database

I. Laboratory Measurements

Roland Schermaul,* Richard C. M. Learner,*,[1] David A. Newnham,† R. Gary Williams,† John Ballard,† Nikolai F. Zobov,‡,[2] Djedjiga Belmiloud,‡ and Jonathan Tennyson‡

*Laser Optics and Spectroscopy, Blackett Laboratory, Imperial College of Science, Technology and Medicine, Prince Consort Road, London SW7 2BW, United Kingdom; †Atmospheric Science Division, Space Science and Technology Department, Rutherford Appleton Laboratory, Chilton, Didcot, Oxfordshire OX11 0QX, United Kingdom; and ‡Department of Physics and Astronomy, University College London, Gower Street, London WC1E 6BT, United Kingdom

E-mail: david.newnham@rl.ac.uk, gary.williams@rl.ac.uk, j.ballard@rl.ac.uk, j.tennyson@ucl.ac.uk

Received November 30, 2000; in revised form April 26, 2001

New laboratory measurements are presented for the near-infrared and visible spectrum (8600–15 000 cm^{-1}) of water vapor. Spectral line parameters, principally intensities and air-broadening coefficients, are derived from Fourier transform spectroscopic measurements at high resolution (0.03 cm^{-1}), a range of optical path lengths (5–513 m), and temperatures of both 252 and 296 K. Experimental line parameters are derived for 5034 assigned transitions and thorough error analysis shows parameter errors of less than 2.5% for one-third and less than 5% for over half of the lines. Calculated spectra, derived using these line parameters, reproduce the original spectra to within 2%. A comparison of the line intensities with those in the HITRAN-96 database identifies large errors in the latter with random differences that exceed a factor of two for many lines, and systematic differences between 6 and 26% depending on the water band under consideration. The recent corrections to the HITRAN database by Giver *et al.* (*J. Quant. Spectrosc. Radiat. Transfer* **66, 101–105** (2000)) do not remove these discrepancies and the differences change to 6–38%. The new data are expected to substantially increase the calculated absorption of solar energy due to water vapor in climate models.

Key Words: water vapor; near-infrared and visible spectrum; line intensities; air-broadening coefficients.

1. INTRODUCTION

Water is a superficially simple molecule that has a very complex spectrum. It is one of a small number of atmospheric molecules that absorb significant amounts of visible and near-infrared radiation—radiation at wavelengths near the maximum of the solar emission spectrum. It thus has a major influence on radiation transfer in the terrestrial atmosphere and understanding its absorption properties is essential for climate studies. Model calculations of the Earth's climate rely on molecular databases, of which HITRAN-96 (*1*) is the most used, to provide information about the spectral properties of molecules in the atmosphere. Recently, a problem has been identified in model calculations of atmospheric absorption in both clear and cloudy skies (*2*). Many climate models substantially underestimate the globally averaged short-wavelength absorption compared to atmospheric observations, by as much as 30% of the total atmospheric absorption in the case of clear skies. This anomaly limits our knowledge of the natural atmosphere and our ability to predict the climatological effect of anthropogenic perturbations on the atmosphere. Much research has been directed at identifying atmospheric absorbers additional to those already in the databases to make up the discrepancy, but no critical check of the existing database, especially on water—the primary greenhouse gas and major absorber of solar radiation—has been performed.

The water vapor spectrum has been studied, using both experiment and theory, in far greater detail than that of any other molecule and has, as a consequence, an extensive literature. The main sources of information on the near-infrared and visible spectrum of $H_2^{16}O$ is the work underlying the HITRAN database, which is dominated by laboratory Fourier transform (FTS) measurements made at the National Solar Observatory in Tucson, Arizona, and analyzed by a number of investigators (*3–7*). Some of these data have been (re-)analyzed more recently (*8–10*) and virtually all unidentified lines have been classified, though no significant changes have been made to the line intensities. New

[1] Deceased.

[2] Permanent address: Institute of Applied Physics, Russian Academy of Science, Uljanov Street 46, Nizhnii Novgorod, Russia 603024.

0022-2852/01 $35.00

FTS data, covering the range 13 100–24 100 cm^{-1} and predominantly providing information on line positions only, have been analyzed with the help of ab initio theory (*11*) leading to the assignment of a large number of new transitions. Recent measurements using tuneable, narrow-band, lasers and cavity ring-down spectroscopy (*12–17*) have successfully achieved high signal-to-noise ratios and long absorption path lengths, required to measure weak lines, precise line positions, and broadening coefficients. However, these are limited to a small wavelength range of typically less than 100 nm, and quantitative intensity measurements are still at the proof of principle level. Theoretical methods use two approaches, a pertubative method underlying the early line assignments (*3–6*) and a variational approach (*18, 19*). The latter is a signficant improvement and allows the assignment of many previously unassigned lines as well as the prediction of weak unobserved lines. The calculation of line intensities, however, is still on a level that cannot compare with the experimental data, but is of immediate application to the estimation of intensities of unobserved lines. Similarly, although line-broadening theory has made progress, it is not yet able to make accurate predictions (*20*), though it can suggest the trends of broadening parameters with vibrational and rotational quantum numbers.

As part of a study of satellite-based atmospheric remote sensing applications, relatively high-resolution (0.03 cm^{-1}), long path (up to 513 m) laboratory spectroscopy was used to measure the near-infrared and visible absorption by water vapor at two temperatures (252 and 296 K). Comparison of our measurements with data from the HITRAN-96 database and recent new measurements identified systematic errors in the existing water vapor intensity data. Recently, Giver *et al.* (*21*) reported differences between line intensities from HITRAN-96 and those given in the publications (*3–7*) describing the original measurements. These differences are reported to be due to errors made in the conversion of the original spectroscopic data to the HITRAN database format. Giver *et al.* (*21*) suggested that HITRAN intensities should be increased or reduced depending on the spectral region. The comparison of our new laboratory data with both HITRAN-96 and the update of Giver *et al.* shows that both databases contain significant errors. Here we report new laboratory data for some 5000 of the strongest lines of the water spectrum in the spectral range 8600–15 000 cm^{-1}. Theoretical computations of the water spectrum that support and extend the experimental data will be published in a companion paper. Our new data provide a much improved and upgraded $H_2^{16}O$ database for applications in atmospheric remote sensing.

2. EXPERIMENTAL DETAILS

2.1. Measurements

The near-infrared and visible absorption spectra of water vapor and mixtures of water vapor with synthetic air have been characterized in the laboratory using the combination of a high-resolution Fourier transform spectrometer (FTS) and either a long path (LPAC) or short path (SPAC) absorption cell at the Rutherford Appleton Laboratory (RAL) Molecular Spectroscopy Facility. The Bruker IFS 120HR FTS was configured with a 150-W quartz tungsten halogen source, a dielectric-coated quartz beam splitter, and a silicon photodiode detector as detailed in Ref. (*22*). Optical bandpass filters (fitted with antireflection coated glass wedges) were used to limit the wavelengths of photons arriving at the detector to the spectral range of the measurement for minimization of photon noise. The LPAC, described in detail previously (*23*), was configured with multilayer coated high-reflectance mirrors and antireflection coated glass windows for this work. Measurements of water vapor transmittance spectra were made at high spectrometer resolution ($\delta\tilde{\nu} = 1/L = 0.03$ cm^{-1}, L = maximum optical path difference) and over long optical path lengths ($l = 4.94$–512.75 m) in the spectral region 8500–15 800 cm^{-1} (1180–633 nm). The interferometer aperture diameter was set to match the spectrometer resolution for each experiment. The alignment of the interferometer was optimized and the photometric accuracy tested before carrying out the measurements reported here. The FTS was maintained at a pressure below 0.4 Pa by a turbomolecular pump to minimize the amount of air and water vapor in its optical path. All other optical paths outside of the cells (i.e., the transfer optics between the spectrometer, LPAC or SPAC, and the detector vacuum tank) were evacuated to a pressure below 0.02 Pa by a rotary and diffusion pump combination. The LPAC or SPAC White cell optics were adjusted to give the desired optical pathlength and to optimize the alignment of the output image on the detector. Empty-cell background spectra were recorded before and after each filling of the LPAC. Interferograms were co-added for up to 12 h in order to achieve signal-to-noise ratios (S/N) of up to 1000 : 1. Boxcar apodization and Mertz phase correction were applied to all of the measured interferograms.

Details of the gauges used to measure gas temperature, pressure, and humidity within the cells are given in Table 1. The platinum resistance thermometers (PRTs) used in the LPAC during this work have been shown (*23*) to give consistent and representative measurements of the temperature of gases contained within the LPAC inner vessel. Readings were logged every 30 min. Temperatures of the gas in the SPAC were measured using a set of 6 thermistors (logged every 15 min). The 10- and 1000-Torr Baratron pressure gauges were used during sample preparation and throughout the measurements with either cell. The atmospheric pressure reading of the 1000-Torr Baratron was compared with that of a precision aneroid barometer. The low-pressure readings of the 10-Torr gauge were checked by measuring identical pressures with both Baratron gauges. Relative humidity (RH) was measured with two humidity gauges positioned at opposite ends of the LPAC or by one sensor in the baseplate of the SPAC. The local vapor temperature at the humidity gauges was recorded using PRTs integrated into the sensor.

TABLE 1
Details of Gas Temperature, Pressure, and Humidity Sensors

Measurement	Manufacturer and type	Stated uncertainty
Temperature:		
LPAC:		
Platinum Resistance Thermometers (average of 14)	Heraeus/Nucleotrohms, calibrated four-wire	±0.3 K
Data logger	Philips, PM8237A	±0.4 K
SPAC:		
Thermistors (average of 6)	RS Components, 10 kΩ n.t.c. curve-matched	±0.2 K
Signallogger-PC	Laplace Instruments	±0.3 K
Pressure:		
Baratrons:		
0-10 hPa	MKS, 390 (10 Torr)	±0.08 % of reading
10-1000 hPa	MKS, 390 (1000 Torr)	±0.08 % of reading
Barometer:		
Atmospheric	Negretti, M2236A	±40 Pa
Humidity:		
Relative humidity (RH)	Vaisala, HMP234	
0-90 % RH		±1 %
90-100 % RH		±2 %
Temperature	Vaisala, HMP234	±0.1 %

The spectra were recorded for both pure water vapor and mixtures of water vapor and synthetic air at two temperatures (252 and 296 K) and at three LPAC path lengths (32.75, 128.75, and 512.75 m) as well as one SPAC path length (4.938 m). Water vapor samples were prepared from liquid water using a clean glass vacuum line and purified to remove dissolved air using freeze–pump–thaw cycles. Agreement between the humidity sensor and pressure gauge readings (to within the humidity sensor accuracy) confirmed the purity of the water vapor under study. After an initial period of approximately 30 min, sample pressures remained stable over the period of measurement, indicating that adsorption processes at the cell walls had reached equilibrium. Purity certified "zero" grade synthetic air (Air Products Ltd, 21% oxygen, 79% nitrogen) was used to make water vapor mixtures at a total pressure of approx. 1000hPa. Mixtures were made by rapidly flowing zero air into the LPAC/SPAC after filling it with water vapor. Despite the turbulent flow of the air into the absorption cell, the humidity gauges indicated that at room temperature a stabilization period of 3 h was required to achieve uniform mixing of the water and air. At 252 K the stabilization time was extended to between 8 and 12 h. The total pressure and relative humidity were recorded at suitable intervals during measurements.

2.2. Experimental Conditions

The three experimental parameters, temperature T, sample pressure p, and absorption path length l, describe the conditions of an individual measurement and their uncertainties determine to a large part the achievable precision of the spectral line parameters. Therefore, the measurements of the experimental conditions are evaluated here.

2.2.1. Temperature

The temperature inhomogeneity of the LPAC at a given time was smaller than ±0.2 K at 296 K and smaller than ±0.4 K at $T = 252$ K. During an observation, the LPAC temperature drifted by typically less than 0.5 K. The individual thermistor readings of the SPAC temperatures agreed to within 0.7 K at any time and no measurable temperature drift was observed during the experiments. A comparison of these readings with the temperature readings provided by the humidity sensors showed the latter to give systematically higher values. The discrepancies were less than 1 K at room temperature, but at low temperature increased to 5 and 7 K for the water–air and pure water measurements, respectively. These differences can be explained by insufficient thermal isolation of the humidity sensors, thus causing an increasing difference with decreasing cell temperature while the higher gas pressure of the water–air mixture relative to the pure water measurements caused a higher cooling effect on the humidity sensors. Given the lower reliability of these readings, only the PRT and thermistor readings were used to derive the mean gas temperatures for the observations.

The spatial and temporal mean temperature for given spectrum measurement was calculated as the average of all observations over the time of the measurement. The uncertainty of the mean temperature has two contributions: the uncertainty in the temperature reading and the uncertainty arising from the spatial and temporal temperature variations. The effect of the latter on the mean temperature can be approximated by the standard error of the mean value, which is in all cases smaller than 0.1 K. The temperature uncertainty is mainly determined by the uncertainty in the reading, which can be estimated to be the sum of the quoted accuracies of the sensor and the data logging system. This yields an uncertainty of 0.7 K for the PRT readings of the LPAC and 0.5 K for the thermistor readings of the SPAC. The results are summarized in Table 2.

2.2.2. Pressure

The pressure measurements for both the LPAC and SPAC observations made using MKS Baratron capacitance gauges were taken at the beginning and the end of each measurement. Additionally, the water partial pressures, p_{H_2O}, in the mixtures with air were determined from the relative humidity and the tabulated saturation vapor pressure of water at the temperature of the humidity sensor (*24*). The 10-Torr gauge provided a measure for the initial pure water pressure. After air was added to make a total pressure of approx. 1000 hPa, the 1000-Torr gauge gave the total pressure and the humidity sensors the actual water partial pressure in the mixture. In each case the mean of the start and end readings were calculated. For pure water measurements both types of sensors gave a measure for the water vapor pressure. The errors of the individual readings were estimated to be the sum of the accuracy of the type of sensor as specified by the manufacturer and the temporal change in pressure. A full error analysis using the monitored pressure values yielded typical

TABLE 2
Experimental Conditions of the Water Vapor Measurements: (Exp. A) 8500–15 000 cm^{-1}, (Exp. B) 12 800–15 800 cm^{-1}

#	Sample	Exp.	l (m)	T (K)	p_{H_2O} (hPa)	p_{tot} (hPa)[a]
1	H_2O	A	4.938 (13)	294.9 (5)	9.459 (44)[a]	9.459 (44)
2	H_2O/Air	A	4.938 (13)	295.3 (5)	8.83 (28)[b]	999.29 (97)
3	H_2O	A	32.75 (6)	294.4 (7)	10.017 (15)[a]	10.017 (15)
4	H_2O/Air	A	32.75 (6)	296.2 (7)	9.10 (23)[c]	1003.6 (16)
5	H_2O/Air	B	32.75 (6)	296.0 (7)	9.25 (14)[c]	1000.0 (12)
6	H_2O	A	128.75 (18)	295.7 (7)	10.008 (11)[a]	10.008 (11)
7	H_2O/Air	A	128.75 (18)	296.4 (7)	9.07 (23)[c]	999.9 (14)
8	H_2O/Air	B	128.75 (18)	296.1 (7)	9.18 (15)[c]	1000.0 (11)
9	H_2O	A	512.75 (66)	295.6 (7)	10.094 (11)[a]	10.094 (11)
10	H_2O/Air	A	512.75 (66)	296.4 (7)	9.08 (21)[c]	1001.3 (10)
11	H_2O	B	512.75 (66)	295.8 (7)	10.003 (11)[a]	10.003 (11)
12	H_2O/Air	B	512.75 (66)	296.4 (7)	8.96 (42)[c]	1000.5 (13)
13	H_2O	A	128.75 (18)	252.0 (7)	0.809 (2)[a]	0.809 (2)
14	H_2O/Air	A	128.75 (18)	252.1 (7)	0.717 (10)[c]	998.7 (10)
15	H_2O	A	512.75 (66)	251.0 (7)	0.816 (6)[a]	0.816 (6)
16	H_2O/Air	A	512.75 (66)	251.1 (7)	0.713 (11)[c]	998.9 (11)

[a] Pressure measurements using the MKS Baratron gauges.
[b] Pressure determined from the spectral analysis.
[c] Pressure measurements using the humidity sensors.
Note: The numbers in parentheses are the error estimates in units of the last digit quoted.

uncertainties of ±0.010 hPa for the 10 Torr gauge and ±1.0 hPa for the 1000 Torr gauge at full-scale reading. The errors of the partial pressures derived from the humidity readings were typically 0.1–0.2 hPa.

Systematic differences between the Baratron readings and the humidity sensors were observed with the latter always giving smaller values. Several effects contribute to these discrepancies depending on the sample type, pressure and temperature. For measurements of pure water samples at room temperature the pressure readings agreed within 0.5%, while discrepancies of up to 6% were observed at low temperature. The discrepancies between the two sensors increased for the water–air measurements to 7.5–10.4% at room temperature and to up to 12% at low temperature. Much effort has been expended in trying to resolve this lack of agreement and the following explanations were found:

At low temperature, part of the problem is due to the insufficient thermal isolation of the humidity sensors. The large temperature differences observed cause an erroneous evaluation of the relative humidity by the sensor itself. This effect is less critical for the water–air mixtures as the higher gas pressure contributes to additional cooling of the sensors. This explains why the low-temperature discrepancies are much closer to the room temperature discrepancies for the water–air mixtures than they are for the pure water measurements at low pressure.

The most probable cause of the large discrepancies for the water–air mixtures is that the admission of 1000 hPa air via a single entry valve into a cell containing 10 hPa of water vapor may sweep some of the water into the corners of the cell. The water does not emerge from these places and a complete mixing does not happen, even after several hours. Therefore, we have chosen to accept the humidity sensor readings, a decision supported by a comparison of the low- and high-pressure spectral analyses.

The discrepancies were even worse for the SPAC measurements with water partial pressures of 3.18 (15) hPa and 7.09 (8) hPa compared to the initial water pressure of 9.39 (9) hPa in a 1000 hPa water–air mixture. In the case of the SPAC measurements additional effects must cause the big differences, one of which may be the placement of the humidity sensors inside the pipework of the cells base-plate rather the cell itself. These readings were considered unreliable and the water partial pressure was derived from the spectral analysis. A summary of the derived pressure values is given in Table 2.

2.2.3. Absorption Path Length

The path through the multipath cells has two components: a main multireflection path between the cell mirrors and additional paths from the entrance window to the first focus and from the final focus to the exit window. The main mirror separation for the LPAC is $R = 8000\,(10)$ mm and for the SPAC $R = 400\,(1)$ mm. The small additional component is $d = 746\,(20)$ mm for the LPAC and $d = 138\,(1)$ mm for the SPAC. The total path l is given by $l = (2n + 2)R + d$, where $(2n + 2)$ is the number of traversals of the light beam inside, the cell. This gives path lengths of 32.75 (6) m, 128.75 (18) m, and 512.75 (66) m for the LPAC measurements and 4.938 (13) m for the SPAC observations.

3. DATA ANALYSIS AND RESULTS

3.1. Baseline Correction

Fourier transformation of each observation yields a single-beam absorption spectrum with the absorption lines sitting on an underlying background signal. This background signal was removed, to a first approximation, by calculating the average of the empty-cell spectra recorded before and after each sample measurement and then taking the ratio of the full to empty cell signals to give the corresponding transmittance spectrum, $T(\tilde{\nu})$. Due to changes in the lamp output during the 12-hour observations and other small effects, the empty-cell spectra are not an exact match of the underlying background signal and systematic departures of the baseline from its true value of 100% transmittance still remain after ratioing. These discrepancies are wavenumber dependent and are typically of the order of up to 1–2%. An example is shown in Fig. 1.

An improved baseline was derived by cubic spline interpolation through a set of carefully chosen points along the baseline. These points were taken at points on the baseline where there is no obvious absorption by water lines. This is relatively straightforward for the water vapor only spectra, where the lines are sharp and generally well separated. The task is far more difficult for the spectra of water–air mixtures, where the lines are

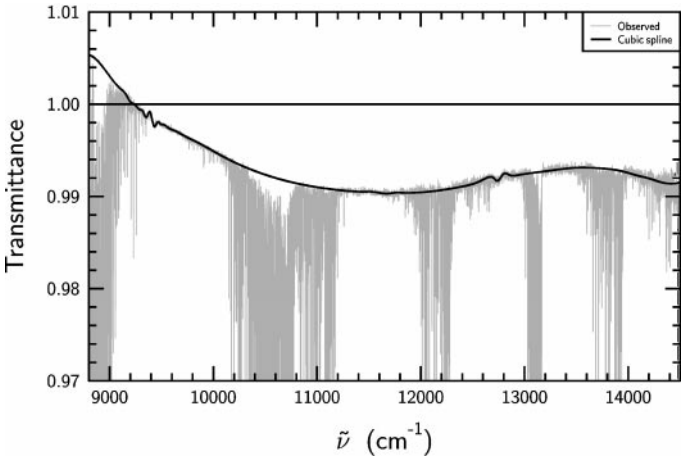

FIG. 1. Expanded baseline region of a transmittance spectrum showing the remaining wavenumber-dependent deviation from 100% transmittance after ratioing of the observed single-beam absorption spectrum with an empty-cell background spectrum. Additional baseline correction is necessary and was achieved by interpolation from chosen datapoints along the spectral baseline where no obvious absorption by water was found.

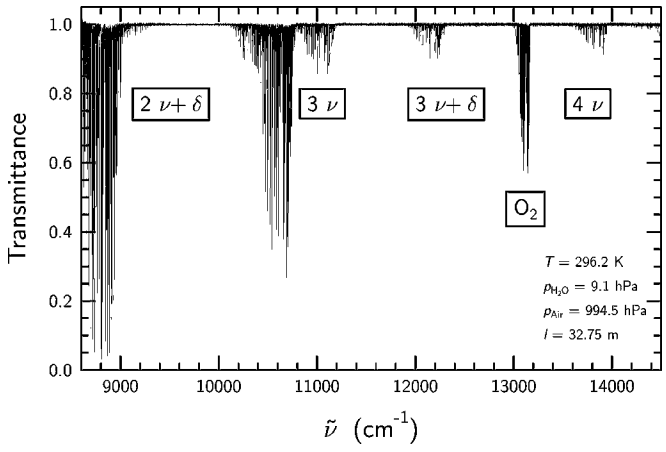

FIG. 2. Near-infrared and visible transmittance spectrum of a water–air mixture showing the different water polyads and the oxygen *A*-band in this spectral region.

pressure-broadened and the spectrum contains a large number of blended lines. In regions of strong absorption there are large intervals where no clear, unabsorbed windows can be seen; a smoothly varying cubic spline function was used to give the best estimate of the continuum level across these regions. The procedure of baseline correction was performed in several steps to achieve the best possible spectral baseline for the observed transmittance spectrum. Independent estimates of the baseline at two laboratories (Imperial College and RAL) show that the result is typically accurate to better than 10% of the peak-to-peak noise level, which corresponds to less than 0.1% in transmittance. The final transmittance spectra were converted to absorbance spectra according to $A(\tilde{\nu}) = -\ln[T(\tilde{\nu})]$ for input to the spectral line analysis. One of the observed near-infrared and visible water-air transmittance spectra is shown in Fig. 2, the spectrum covers the four water polyads $2\nu + \delta$, 3ν, $3\nu + \delta$ and 4ν.[3] Separate spectra were derived for the region 12 800–15 800 cm^{-1}, using a narrower optical pass band to reduce the the noise level.

3.2. Line Parameter Retrieval

The line parameters of the individual transitions were determined from the absorbance spectra using an interactive least-squares line-fitting procedure that is part of the GREMLIN spectrum analysis software (*25*), which uses a point-by-point fit to determine a four-parameter Voigt profile. The general aim was to fit Voigt line profiles to all lines, such that the residuals of the fit were indistinguishable from the noise. This was usually possible, except when a line was so strong that the peak absorbance approached saturation, or when the wavenumber separation of a pair of lines was so small that the least-squares routine could not find a stable two-line solution. Saturation was the more common problem in the low-pressure spectra and blending was the principal problem in the high-pressure spectra where simultaneous fitting of up to several tens of lines was necessary. A typical result is shown in Fig. 3.

The molecular lineshape was assumed to be a Voigt line profile, i.e., a convolution of Lorentzian (pressure-broadened) and Gaussian (Doppler-broadened) contributions. Although the Doppler contribution to a Voigt profile caused by the motion of the particles can generally be calculated and only the Lorentzian being fitted, the effect of collisional narrowing (*12*, *13*, *16*) is strong enough at atmospheric pressure to seriously distort

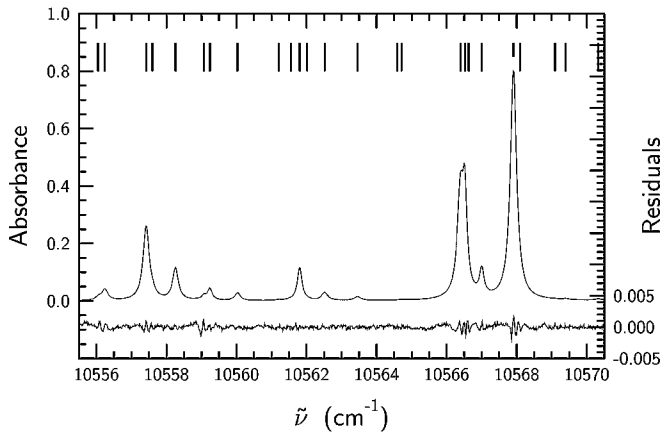

FIG. 3. Results of a spectral line-fit. The vertical markers indicate the fitted lines in the spectrum. The residuals of the fit are shown as the trace on an expanded scale below.

[3] A polyad, denoted as $n\nu$, is a set of superposed bands for which $n = v_1 + v_2/2 + v_3$, where v_1, v_2, and v_3 are the vibrational quantum numbers of the excited state. If v_2 is odd, n is the integer part of the sum, and a δ is added to the notation.

standard Voigt line profiles; see (*26*). Collisional narrowing has been observed for the water molecule for a small number of lines (*12, 13, 16*) and found to vary between 0.005–0.015 cm^{-1} atm^{-1}. Without exact knowledge of the latter for the majority of lines, the effect can, however, not generally be simulated and included in our line fits. Although there are more complex line profiles based on hard- and soft-collisional models that include collisional narrowing, it has been shown that "generalized" Voigt profiles, profiles for which both Lorentzian and Gaussian contributions are adjusted, fit observed lineshapes equally well [16]. Furthermore, "generalized" Voigt profiles are much faster to compute and less prone to numerical correlations, making them the preferred option for this study. These are factors of particular importance for the fitting of a complex spectrum with thousands of lines and a large number of blends. This data reduction procedure has been used successful to study the oxygen A-band (*26*), where further discussion can be found.

In order to achieve the best fit of the lineshapes and to determine precise intensities, "generalized" Voigt profiles were used. This procedure has, however, a negative effect on the line broadening information. Whereas the Lorentzian and Gaussian contributions are clearly defined for a "standard" Voigt profile, with the Gaussian contribution given by the temperature and the mass of the absorber molecule and the Lorentzian contribution given by the pressure broadening, the use of the "generalized" Voigt profile degrades the physical meaning of the two contributions. In such a case, a change in the damping parameter (the ratio of the Lorentzian contribution to the total line width) may include second order effects that change the line shape. Such effects may have technical reasons like line blending or small baseline errors, but may also have a physical cause such as an instrumental line shape contribution or collisonal narrowing. The effect of the instrumental line shape on the line fit of the air-broadened water spectra was found to be negligibly small, but was included through filtered line fits for pure water spectra. Details on how the Lorentzian contribution to the line widths were retrieved are given in section 3.2.3.

The set of line parameters retrieved for a given line consisted of the line position, $\tilde{\nu}_{nm}$,[4] the peak absorbance, A_p, the integrated absorbance evaluated as the integral over the fitted line profile, A_I, the full line width at half maximum, FWHM, and the damping parameter, D. The uncertainties in the spectral line parameters were estimated using the expressions [25]

$$\frac{\Delta\tilde{\nu}_{nm}}{\mathrm{FWHM}} \sim \frac{\Delta\mathrm{FWHM}}{\mathrm{FWHM}} \sim \frac{\Delta A_I}{A_I} = \frac{k_p}{(S/N)\sqrt{N_W}}, \qquad [1]$$

where the signal-to-noise ratio (S/N) is given by the ratio of the peak absorbance to the *rms* noise at the line position and N_W is the number of statistically independent points in a line width, which can be determined from the line width and the spectral resolution. The parameter k_p is a constant for a given set of line parameters, where the index p indicates either $\tilde{\nu}_{nm}$, FWHM or A_I. The above data sets are well represented by $k_{\tilde{\nu}_{nm}} = 0.8$, $k_{\mathrm{FWHM}} = 2.5$, and $k_{A_I} = 2.0$.

As the initial aim of this study was to measure air-broadening coefficients, the analysis described here used only the water–air spectra to derive the spectral line parameters for the four water polyads. Although the pure water spectra measured here contain valuable information, many of the spectral lines were saturated or approaching saturation in these spectra even at the shortest path length and were thus unusable. The pure water spectra were used to solve the problem of the determination of the water partial pressure in the water–air mixtures and to identify the number of components of blended lines in the air-broadened spectra. As the observed integrated absorbance is a direct measure of the amount of water in the optical path, this parameter was used to investigate the discrepancies in the pressure measurements. Integrated absorbances for water only and water–air observations, which were observed using the same initial cell filling of water, should give the same integrated absorbances, unless the amount of water in the path changed during the process of filling the cell with air. A direct comparison is complicated by the large difference in peak absorbances between such two spectra—medium strong lines in the water–air spectrum are usually saturated in the pure water spectrum, while medium strong lines in the pure water spectrum are typically weak lines in the water–air spectrum. However, a subset of 130 well-resolved, unsaturated lines in the 32-m room temperature spectra was found to provide a reliable comparison. The ratio between the integrated absorbances of high- and low-pressure spectra yielded a value of 0.93 ± 0.07, which is consistent with the differences observed between the Baratron gauges and the humidity sensors. This added confidence in the choice of the humidity sensor readings for the determination of water partial pressures.

The output from the fitting procedure and the error calculations were then used to derive the line parameters for each individual spectrum and some aspects are discussed below in terms of the individual line parameters.

3.2.1. Line Positions and Assignments

The line positions derived from the fits of the water–air spectra recorded at 1000 hPa through this study are affected by two factors. First, although the Fourier transform spectrometer allows an internal calibration through the use of a helium–neon laser, which determines the wavenumber limits of the measured spectra, additional calibration is usually required for absolute wavenumber accuracy due to second order effects (small misalignments, etc.). Second, pressure-induced line shifts usually cause the lines to shift to smaller wavenumber with increasing sample pressure. Air-shifts for water have been found (*12, 13, 16*) to be of the order of $\delta_{\tilde{\nu}_{nm}} = 0.010$–$0.025\,\mathrm{cm}^{-1}\,\mathrm{atm}^{-1}$ and are dependent on the vibrational–rotational transition involved. As absolute line positions were not the primary aim of this study and are available from previous work, the spectra remained

[4] m indicates the lower level and n the upper energy level of a transition.

uncalibrated and further evaluation was not pursued. Line positions derived from energy levels were used together with *ab initio* molecular theory to make quantum number assignments for the transitions. Details of the theoretical methods, the assignments, and the calculation of weak unmeasured lines will be given in the companion paper to this study (*27*).

3.2.2. Integrated Line Intensities

Integrated line intensities were derived from the integrated absorbances according to

$$\bar{S}_m^n = \frac{T}{T_0\, L_0} \times \frac{A_I}{p_{\mathrm{H_2O}}\, l}, \qquad [2]$$

where the Loschmidt number $L_0 = 2.686\,763\,(23) \times 10^{19}$ cm^{-3} atm^{-1} gives the number of particles of an ideal gas at standard pressure $p_0 = 1$ atm and $T_0 = 273.15$ K. The intensities are given in units of cm molecule^{-1} (HITRAN units). No distinction was made between the contributions from the different isotopomers of the water molecule. The error estimates of the line intensities were based on the uncertainties in the individual parameters and calculated via standard error analysis.

3.2.3. Air-Induced Pressure-Broadening Coefficients

The derivation of air-induced pressure-broadening coefficients requires the evaluation of two effects: first the contribution of pressure broadening to the line profile (the Lorentzian contribution) and second the identification of air-induced and self-induced broadening components of the Lorentzian.

Calculation of the Lorentzian contribution. The total pressure-broadening coefficient γ_{L}(tot), independent of the type of broadening gas, is given by the Lorentzian contribution to the line profile, FWHM$_{\mathrm{L}}$, and the total pressure in the sample cell,

$$\gamma_{\mathrm{L}}(\mathrm{tot}) = \frac{\mathrm{FWHM_L}}{2\,p_{\mathrm{tot}}}. \qquad [3]$$

As mentioned above, the damping parameter derived from a line fit loses its true physical meaning for a "generalized" Voigt profile and the Lorentzian contribution can only be extracted approximately. It follows that we are left without direct information on the Lorentzian contribution to the line profile and have to consider collisional narrowing in some way in order to determine the best possible broadening coefficients from the total linewidth. As collisional narrowing parameters have only been measured for a small number of water lines, an empirical estimate was made for its contribution to the linewidth. Simulations show that for a "standard" Voigt profile and pressure-broadening coefficients in the range γ_{L}(tot) = 0.050–0.100 cm^{-1} atm^{-1} damping parameters $D = 0.94$–0.98 are expected for the water–air spectra of this study at room temperature. As the Doppler linewidth decreases with temperature, damping parameters even closer to 1.0 are expected at lower temperature. If collisional narrowing of the Doppler width of order 0.005–0.015 cm^{-1} atm^{-1} is included in the simulation, damping parameter of $D = 0.96$–1.0 are calculated. This means that assuming FWHM$_{\mathrm{L}}$ to be equal to the total line width would give errors of up to 4% in the broadening coefficients. Given that a large fraction of the observed water lines have air-broadening coefficients around a mean value of $\gamma_{\mathrm{L}} = 0.080$ cm^{-1} atm^{-1}, a mean damping parameter of $D = 0.99$ is expected for an average collisional narrowing of 0.010 cm^{-1} atm^{-1}. Thus, assuming a damping parameter of $D = 0.99$, the Lorentzian contribution to the line profile was estimated to be FWHM$_{\mathrm{L}} = 0.99 \times$ FWHM with a mean uncertainty of 1%. This procedure should, however, be considered an interim solution until collisional narrowing parameters become available for the majority of the water lines.

Derivation of air-broadening coefficients. The total pressure broadening γ_{L}(tot) has two contributions, one from broadening by air molecules, γ_{L}(air), and one from self-broadening from other water molecules, $\gamma_{\mathrm{L}}(\mathrm{H_2O})$:

$$\gamma_{\mathrm{L}}(\mathrm{tot}) \times p_{\mathrm{tot}} = \gamma_{\mathrm{L}}(\mathrm{H_2O}) \times p_{\mathrm{H_2O}} + \gamma_{\mathrm{L}}(\mathrm{air}) \times p_{\mathrm{air}}. \qquad [4]$$

The simple addition of the two terms is justified because both terms make the absorption Lorentzian. In order to determine the air-broadening coefficient from the total broadening, the self-broadening coefficient as well as the partial pressures needs to be known. Although the HITRAN-96 database (*1*) contains self-broadening coefficients for water, not all lines measured in this study are listed and a large fraction of the coefficients listed are from theoretical rather than experimental data. In order to provide a consistent set of air-broadening coefficients, a procedure was adopted that applies an estimated mean ratio between the air- and self-broadening coefficients for water. Two studies have been made to compare self-broadening of water with nitrogen-broadening (*13*, *28*, *29*), giving a mean ratio of $\gamma_{\mathrm{L}}(\mathrm{H_2O})/\gamma_{\mathrm{L}}(\mathrm{N_2}) = 4.61(11)$. These and other studies (*30*–*32*) also measured the mean ratio between air- and nitrogen-broadening, which if combined yields a mean ratio of $\gamma_{\mathrm{L}}(\mathrm{air})/\gamma_{\mathrm{L}}(\mathrm{N_2}) = 0.897(5)$. It follows that the mean ratio of self- and air-broadening can be calculated as $\gamma_{\mathrm{L}}(\mathrm{H_2O})/\gamma_{\mathrm{L}}(\mathrm{air}) = 5.14(13)$. Applying this relation together with the partial pressures from Table 1, the air-broadening coefficients were derived from the total broadening parameters. The uncertainties of the final results were calculated using standard error analysis.

Using the two datasets recorded at the two temperatures, the temperature dependence of the measured broadening was evaluated using the expression

$$\gamma_{\mathrm{L}}(T) = \gamma_{\mathrm{L}}(T_r) \times \left(\frac{T_r}{T}\right)^n, \qquad [5]$$

where T_r is the reference temperature (296 K), $T = 252$ K, and n is the temperature exponent. Figure 4 shows a plot of the

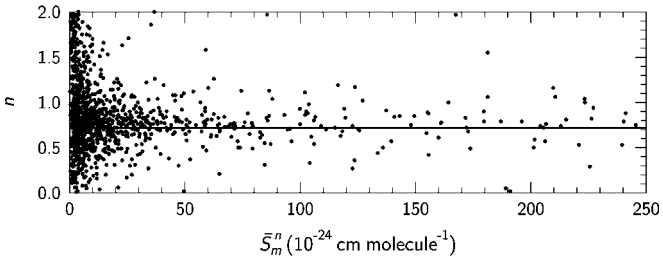

FIG. 4. Air-broadening temperature exponent as a function of line intensity. The horizontal line indicates a weighted average of $n = 0.72 \pm 0.15$ derived from lines above a lower intensity limit of 50×10^{-24} cm molecule^{-1}.

derived temperature exponents versus line intensity. The scatter of the datapoints increases with decreasing intensity, indicating a large effect of the signal-to-noise ratio on the derivation of n. Due to the nonlinear relation, small errors in broadening coefficients can have large effects on the derived n value. An almost constant range of n values between $n = 0.02$ and 1.3 was observed for intensities above 50×10^{-24} cm molecule^{-1} and indicates a dependence on the particular transition, although no clear systematic was found. Using only values above this intensity limit, a weighted mean of $n = 0.72$ with a standard deviation of ± 0.15 was derived. Given the large error of the mean temperature exponent, a value of $n = 0.68$ as used in HITRAN-96 (*1*) was adopted for our linelists until more precise data on the temperature exponent become available.

3.2.4. Compilation of a Combined Line Parameter List

In the final step of the data reduction the line parameter lists derived from each individual spectrum at a given temperature were merged. Transitions with the same assignment were matched and critically assessed for quality by visual comparison of the individual parameters. This process led to a significant number of reassignments, identifications of blends, and lines approaching saturation, and rejections of lines. Finally, a weighted average for each line parameter of a given transition was calculated. The inverse square of the uncertainty of the parameter was used as its weight. The final error of the parameter was given by the square root of the sum of the weights of the parameters contributing to the average.

A third and crucial check of the results was performed by comparison of spectrum simulations with the observed spectra. The water spectrum was modeled in each case for the experimental conditions of the observed spectrum. This process identified a small number of remaining problems, principally weak line blends, which were rectified to produce the final line parameter lists for the two temperatures of the experiments. The data derived from the low-noise 12 800–15 500 cm^{-1} spectra (Experiments B) were also used to reconstruct the more noisy end of the experiment A spectra. The agreement helps to confirm pressure measurements used in the analysis. A summary (of over 11 000 line profile measurements) is given in Table 3. The combination of the two final datasets at room and low temperature requires considerable theoretical input (assignments, lower level energies, partition function) and is discussed in the companion paper (*27*). The line lists are available by file transfer from the authors or on CD-ROM from the European Space Agency (under the reference ESTEC Contract 13312/99/NL/SF). It should be noted that, in a spectrum with much line blending, the parameters of many of the weak lines are strongly influenced by the line wings of very much stronger lines. Data on lines with intensities of less than 5×10^{-24} cm molecule^{-1} should be used with caution. It is for this reason that the comparison with theory presented in the companion paper (*27*) uses only 4155 of the 5034 lines in the experimental list.

A statistical analysis of the parameter errors shows a distribution that is systematically dependent on the total absorption strength of a given polyad. If both the line intensity and the air-broadening coefficient for room temperature data are combined, the following systematic is found:

Error	$2\nu + \delta$	3ν	$3\nu + \delta$	4ν
<2.5%	35%	47%	24%	16%
2.5–5%	18%	20%	23%	21%

Each percentage value gives the proportion of the line parameters for a given polyad which have errors smaller than 2.5% or between 2.5 and 5%. In general, there is a decrease in the proportion of parameters with errors smaller than 2.5% for increasing polyad, which follows the decrease of absorption strength in the polyads from the $2\nu + \delta$ to the 4ν polyad. This coincides with the fact that strong line errors are, to first order, determined by the error in the pressure measurement which is smaller than 2.5%, while weak line errors are determined by the signal-to-noise ratio of the lines. Therefore, the proportion of lines with errors between 2.5 and 5% increases with increasing polyad. The only exception is an increase of the proportion of lines with errors below 2.5% for the $2\nu + \delta$ and 3ν polyad. As the spectral range measured only covers the upper end of the $2\nu + \delta$ polyad, it contains a higher proportion of weaker lines compared to the 3ν polyad.

TABLE 3
Summary of the Number of Lines Fitted for a Given Spectrum and Polyad and the Size of the Combined Line Lists

Temperature	Spectrum	l (m)	$2\nu + \delta$	3ν	$3\nu + \delta$	4ν
296 K	2	4.94	100	348	–	–
	4	32.75	193	375	12	–
	7	128.75	418	1801	479	–
	8	128.75	–	–	–	408
	10	512.75	592	1834	828	–
	12	512.75	–	–	–	1023
252 K	14	128.75	288	805	96	67
	16	512.75	334	920	151	126
		Combined	706	2447	899	982

The fact that a large proportion of line parameters for all polyads have errors exceeding 5% does not translate into larger errors in absorption cross-sections, which can be derived from the parameters. The strong lines, which contribute more than 98% of the total intensity of a polyad, mainly determine the uncertainties in the cross-sections. These fall into the category with errors smaller than 2.5%, while weak lines make up the proportion of line parameters with bigger errors. Therefore, absorption cross-sections derived from this data will meet an overall accuracy of better than 5%.

3.3. Discussion

Spectral line parameters, principally line intensities and air-broadening coefficients, for approximately 5000 lines in the 8600–15 000 cm^{-1} spectrum of water vapor were derived for two temperatures, $T = 252$ and 296 K. All lines were assigned to form an improved and upgraded $H_2^{16}O$ database for application in atmospheric remote sensing and climate studies. In this respect, it is important to compare the new results with the existing data, especially with HITRAN-96 (*1*) as the most used spectroscopic database in atmospheric science.

3.3.1. Line Positions

A comparison of the observed line positions from this study with the line positions in the HITRAN-96 database confirms the points made in section 3.2.1. Systematic differences of as much as -0.040 cm^{-1} for the majority of lines with a mean value of -0.020 cm^{-1} between the observed line positions for the water-air mixtures of this study and the HITRAN-96 data were observed. These differences are principally determined by the pressure-induced line shifts. The line positions derived from the low-temperature spectra agreed in general to within ± 0.010 cm^{-1} with the corresponding room temperature values, suggesting that the pressure shifts are not strongly temperature dependent.

3.3.2. Line Intensities

A comparison of the observed integrated line intensities from this study with the line intensities listed in the HITRAN-96 database shows significant systematic differences. As Fig. 5a shows, the dominant effect is a mean 25% offset for the 3ν and $3\nu + \delta$ polyads, an offset that decreases from about 30 to 0% within the $2\nu + \delta$ polyad, and only a very small offset for the 4ν polyad. The scattering within each polyad is quite large; more than $\pm 50\%$. However, as Fig. 5b shows, this scatter is mainly due to the weak lines. Similar results have been found for the low temperature intensities. The ratios between the observed and HITRAN-96 values are similar for both low and room temperature measurements. A summary of the results is given in Table 4. Attempts to explain the difference between the database and the new data lead back to the experimental observations upon which the database is built. These are an extensive series of measurements made using the National Solar Observatory at Kitt Peak

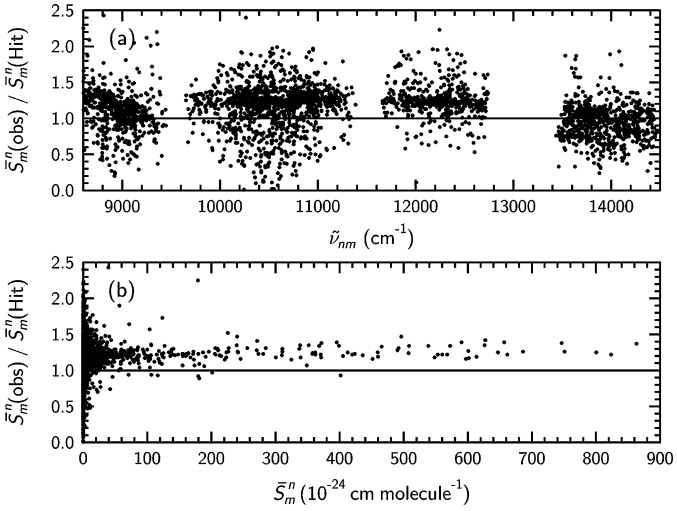

FIG. 5. Comparison of the observed room-temperature integrated line intensities with the HITRAN-96 database: (a) polyad-by-polyad as a function of wavenumber, (b) as a function of the line intensity.

in the early 1980's (*3–7*). The earlier data set concentrated on long paths and so stronger lines were saturated. The simple reduction algorithms used at a time when computing speed was not sufficient to allow detailed line-by-line fitting were most prone to error when treating saturated lines and strong blends. The current work with spectroscopic data covering more than a factor of 100 in path length and the available computing resources needed to fit line profiles to over 10,000 lines make for a considerably more robust analysis. Most significant, judging by the uniformity of line intensity ratios for lines of moderate strength shown in Fig. 5, are systematic errors arising either from the approximations of the line fitting procedure or from the determination of the concentration of water vapor in the absorption cell. The 1980's measurements used precision manometry to measure water vapor pressure and did not use mixed gases. The present work also used precise manometry until observed discrepancies led to a review of technique. Lost, presumably readsorbed water caused a decrease of approximately 10% in the actual partial pressure of a nominal 10-hPa water (in 1000 hPa

TABLE 4

Comparison of Three Sets of Water Band Intensities for the Four Polyads in the Spectral Region 8500–15 800 cm^{-1}

Polyad	$\bar{S}_B$(obs)/$\bar{S}_B$(Hit)	$\bar{S}_B$(Giv)/$\bar{S}_B$(Hit)	$\bar{S}_B$(obs)/$\bar{S}_B$(Giv)
$2\nu + \delta$	1.26	0.92	1.38
3ν	1.21	1.14	1.06
$3\nu + \delta$	1.25	1.09	1.15
4ν	1.06	0.96	1.10

Note. Each entry gives the ratio of band intensities for $T = 296$ K, where $\bar{S}_B$(obs) are the observed data from this study, $\bar{S}_B$(Hit) are the HITRAN-96 data, and $\bar{S}_B$(Giver) are the corrections of Giver *et al.* (*21*) to the HITRAN-96 database.

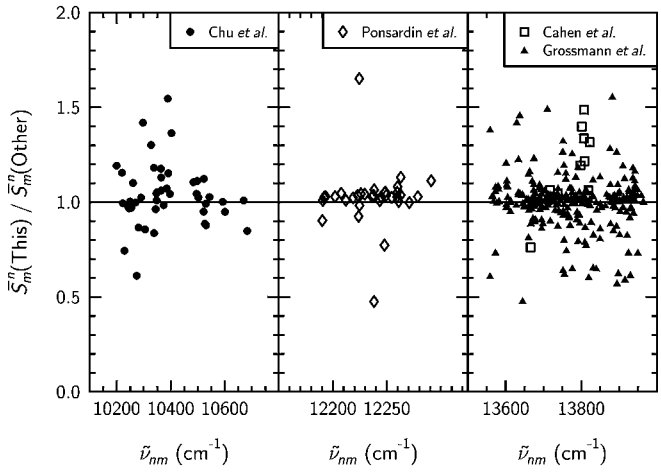

FIG. 6. Comparison of the observed room-temperature integrated line intensities with other data sources for three parts of the spectral region covering the 3ν, $3\nu + \delta$, and 4ν polyads.

air) in the LPAC. The use of pure water at low pressure should diminish pressure errors, but it much emphasizes any line fitting errors in treating strong or saturated lines. This conclusion is very strongly supported by attempts to reconstruct the Kitt Peak spectra using the published line-by-line data. These do not reproduce the observed spectra, in strong contrast to our new data.

Although the recent corrections to HITRAN-96 by Giver *et al.* (*21*) remove some of the errors made during compilation of the database, systematic differences still remain. For instance, although the intensities for the 3ν polyad were systematically increased by about 14%, a further increase of about 10% is required to bring the update into reasonable agreement with the new measurements. The corrections applied to the other polyads are less systematic—intensities in the $2\nu + \delta$ and 4ν polyads were reduced by up to 20% and those for the $3\nu + \delta$ polyad either remained unchanged or increased by 9%. In summary, our new measurements suggest an overall increase above the HITRAN-96 values (Table 4, column 2), while the update of Giver *et al.* (column 3) suggests both increases (3ν and $3\nu + \delta$ polyads) and decreases ($2\nu + \delta$ and 4ν polyads) in intensities.

Comparisons of intensity data of this study with other data sources are given in Fig. 6 and Table 5. The 45 lines for the 3ν polyad measured by Chu *et al.* (*33*) are on average 3(11)% smaller with a large standard deviation. The 35 lines for the $3\nu + \delta$ polyad of Ponsardin and Browell (*16*) are also on average 3(4)% smaller. Grossmann *et al.* (*12*) measured line intensities for 270 lines in the 4ν polyad and found intensities that were on average 9% larger than the corresponding data of Mandin *et al.* (*4*). Given the Giver *et al.* corrections of the compilation errors in HITRAN-96, which is based on the latter dataset in this spectral region, the findings of Grossmann *et al.* are in very good agreement with the band intensity ratio of 1.10 found in this study. A line-by-line comparison of the results of this study

TABLE 5

Comparison of the Observed Room Temperature Integrated Line Intensities and Air-Broadenning Coefficients with Other Data Sources for Three Polyads

Other	Polyad	$\bar{S}_m^n$ ratio (This / Other)	# lines	γ_L(air) ratio (This / Other)	# lines
Chu *et al.* [33]	3ν	1.03 (11)	45	0.88 (8)	25
Ponsardin *et al.* [16]	$3\nu + \delta$	1.03 (4)	35	1.02 (2)	28
Grossmann *et al.* [12]	4ν	1.02 (6)	259	1.05 (4)	123
Cahen *et al.* [34]	4ν	1.20 (18)	12	0.99 (5)	12

Note. The ratios given are the intensity weighted means of the line-by-line ratios using the number of lines as indicated. The number in parentheses are the standard deviations in units of the lost digit quoted.

with Grossmann *et al.* yielded a mean line intensity ratio of 1.02(6). A comparison with a small dataset of 12 lines of Cahen *et al.* (*34*) yields a mean ratio of 1.20(18) for the 4ν polyad, again with a large standard deviation.

We believe that the new data, taken from a much wider range of experimental conditions and buttressed by line-by-line profile fitting and by sophisticated theoretical calculation, are an improvement on the current HITRAN-96 listing.

3.3.3. Air-Broadening Coefficients

A comparison of the air-broadening coefficients with the HITRAN-96 values is shown in Fig. 7. Although a wide scatter similar to that for the line intensities was observed, the general trend shows agreement between the observed and HITRAN-96 values. As for the line intensities, the scattering is due to the many weak lines, while the strong line broadening parameters give mostly ratios within 1.0 ± 0.1. Similar results have been

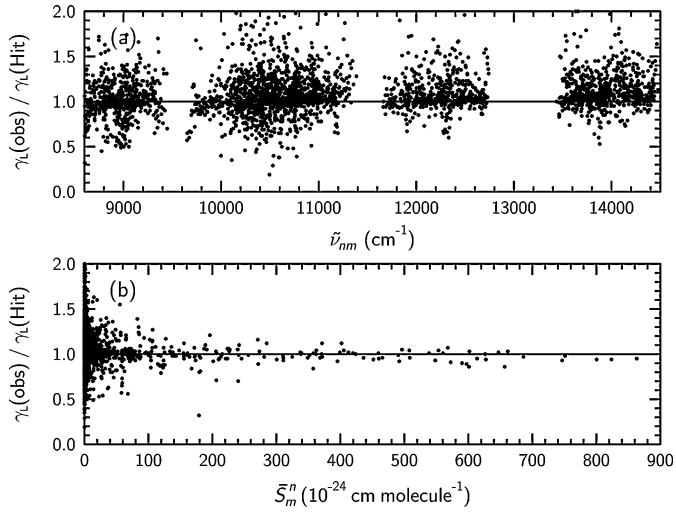

FIG. 7. Comparison of the observed air-broadening coefficients with HITRAN-96 values: (a) polyad-by-polyad as a function of wavenumber, (b) as a function of the line intensity.

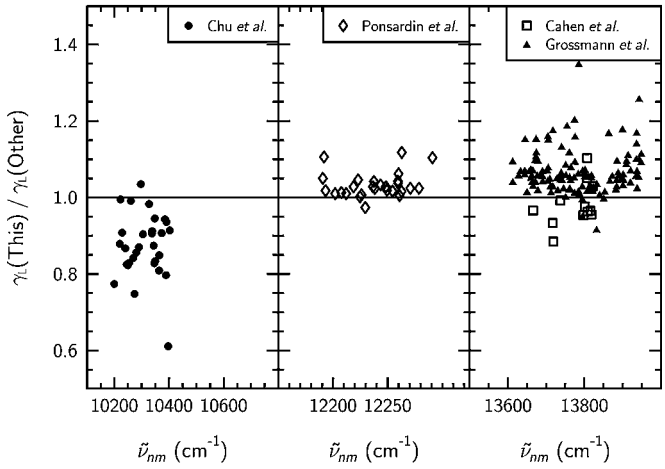

FIG. 8. Comparison of the observed room-temperature air-broadening coefficients with other data sources for three parts of the spectral region covering the 3ν, $3\nu + \delta$, and 4ν polyads.

found for the low-temperature broadening parameters. The ratios between the observed and HITRAN-96 values agree for both room- and low-temperature measurements to within $\pm 10\%$. A line-by-line comparison of the data of this study with air-broadening coefficients derived in other studies is given in Fig. 8. Mean ratios of 0.88(8) for the 25 lines in the 3ν polyad given by Chu *et al.* (*33*), of 1.02(2) relative to the 28 air-broadening coefficients of Ponsardin and Browell (*16*) for the $3\nu + \delta$ polyad, 1.05(4) for the 4ν polyad data of Grossmann *et al.* (*13*), and 0.99(5) for the 12 4ν band lines of Cahen *et al.* (*34*) were derived. The temperature exponent of $n = 0.72(15)$ derived from this study also compares well with the exponent $n = 0.67(13)$ found by Grossmann *et al.* However, the systematic dependence of n on air-broadening coefficients as seen by Grossmann *et al.*, was not as clear from our data.

ACKNOWLEDGMENTS

We thank the U.K. Natural Environment Research Council (Grants GR3/11097, GR3/11674) and the European Space Agency (ESTEC Contract 13312/99/NL/SF) for support. We also thank M. Wickett of Serco Europe Ltd. for undertaking the project management. We have benefited greatly from the work of G. S. Jones-Gilby, who carried out a large part of the basic line fitting computation. Many helpful discussions with J. W. Brault are most gratefully acknowledged.

REFERENCES

1. L. S. Rothman, C. P. Rinsland, A. Goldman, S. T. Massie, D. P. Edwards, J.-M. Flaud, A. Perrin, C. Camy-Peyret, V. Dana, J.-Y. Mandin, J. Schroeder, A. McCann, R. R. Gamache, R. B. Wattson, K. Yoshino, K. V. Chance, K. W. Jucks, L. R. Brown, V. Nemtchinov, and P. Varanasi, *J. Quant. Spectrosc. Radiat. Transfer* **60,** 665–710 (1998).
2. A. Arking, *J. Climate* **12,** 1589–1600, 1999.
3. C. Camy-Peyret, J.-M. Flaud, J.-Y. Mandin, J.-P. Chevillard, J. Brault, D. R. Ramsay, and M. Vervloet, *J. Mol. Spectrosc.* **113,** 208–228 (1985).
4. J.-Y. Mandin, J.-P. Chevillard, C. Camy-Peyret, and J.-M. Flaud, *J. Mol. Spectrosc.* **116,** 167–190 (1986).
5. J.-Y. Mandin, J.-P. Chevillard, J.-M. Flaud, and C. Camy-Peyret, *Can. J. Phys.* **66,** 997–1011 (1988).
6. J.-P. Chevillard, J.-Y. Mandin, J.-M. Flaud, and C. Camy-Peyret, *Can. J. Phys.* **67,** 1065–1084 (1989).
7. R. A. Toth, *J. Mol. Spectrosc.* **166,** 176–183 (1994).
8. J.-M. Flaud, C. Camy-Peyret, A. Bykov, O. Naumenko, T. Petrova, A. Scherbakov, and L. Sinitsa, *J. Mol. Spectrosc.* **183,** 300–309 (1997).
9. J.-M. Flaud, C. Camy-Peyret, A. Bykov, O. Naumenko, T. Petrova, A. Scherbakov, and L. Sinitsa, *J. Mol. Spectrosc.* **185,** 211–221 (1997).
10. O. L. Polyansky, N. F. Zobov, S. Viti, and J. Tennyson, *J. Mol. Spectrosc.* **189,** 291–300 (1998).
11. M. Carleer, A. Jenouvrier, A.-C. Vandaele, P. F. Bernath, M. F. Mérienne, R. Colin, N. F. Zobov, O. L. Polyansky, J. Tennyson, and A. V. Savin, *J. Chem. Phys.* **111,** 2444–2450 (1999).
12. B. E. Grossmann and E. V. Browell, *J. Mol. Spectrosc.* **136,** 264–294 (1989).
13. B. E. Grossmann and E. V. Browell, *J. Mol. Spectrosc.* **138,** 562–595 (1989).
14. D. Li and J. G. Baker, *Rev. Sci. Instrum.* **67,** 1686–1687 (1996).
15. B. A. Paldus, J. S. Harris, Jr., J. Martin, J. Xie, and R. N. Zare, *J. Appl. Phys.* **82,** 3199–3204 (1997).
16. P. L. Ponsardin and E. V. Browell, *J. Mol. Spectrosc.* **185,** 58–70 (1997).
17. B. Kalmar and J. J. O'Brien, *J. Mol. Spectrosc.* **192,** 386–393 (1998).
18. O. L. Polyansky, N. F. Zobov, S. Viti, J. Tennyson, P. F. Bernath, and L. Wallace, *Science* **277,** 346–349 (1997).
19. O. L. Polyansky, N. F. Zobov, J. Tennyson, J. A. Lotoski, and P. F. Bernath, *J. Mol. Spectrosc.* **184,** 35–50 (1997).
20. R. R. Gamache, R. Lynch, and S. P. Neshyba, *J. Quant. Spectrosc. Radiat. Transfer* **59,** 319–335 (1998).
21. L. P. Giver, C. Chackerian Jr., and P. Varanasi, *J. Quant. Spectrosc. Radiat. Transfer* **66,** 101–105 (2000).
22. D. A. Newnham and J. Ballard, *J. Geophys. Res.* **103,** 28801–28816 (1998).
23. J. Ballard, K. Strong, J. J. Remedios, M. Page, and W. B. Johnston, *J. Quant. Spectrosc. Radiat. Transfer* **52,** 677–691 (1994).
24. R. C. Weast and M. J. Astle, "CRC Handbook of Chemistry and Physics: A Ready-Reference Book of Chemical and Phyical Data," 63d ed. CRC Press, Boca Raton, FL, 1982.
25. J. W. Brault, The GREMLIN spectrum analysis software, private communication.
26. R. Schermaul and R. C. M. Learner, *J. Quant. Spectrosc. Radiat. Transfer* **61,** 781–794 (1999).
27. R. Schermaul, R. C. M. Learner, D. A. Newnham, J. Ballard, N. F. Zobov, D. Belmiloud, and J. Tennyson, *J. Mol. Spectrosc.* **208,** 43–50 (2001).
28. J. J. Remedios, "Spectroscopy for Remote Sensing of the Atmosphere," Ph.D. thesis. University of Oxford, 1990.
29. R. R. Gamache, J. M. Hartmann, and L. Rosenmann, *J. Quant. Spectrosc. Radiat. Transfer* **52,** 481–499 (1994).
30. R. S. Eng, P. L. Kelley, A. R. Calawa, T. C. Harman, and K. W. Nill, *Molec. Phys.* **28,** 653 (1974).
31. V. M. Devi, D. C. Benner, C. P. Rinsland, M. A. H. Smith, and B. D. Sidney, *J. Mol. Spectrosc.* **117,** 403–407 (1986).
32. S. D. Gasster, C. H. Townes, D. Goorvitch, and F. P. J. Valero, *J. Opt. Soc. Am.* **B5,** 593–601 (1988).
33. Z. Chu, T. D. Wilkerson, and U. N. Singh, *Appl. Opt.* **32,** 992–998 (1993).
34. C. Cahen, B. E. Grossmann, J. L. Lesne, and G. Leboudec, *Appl. Opt.* **25,** 4268-4271 (1986).